Article

Imbibition and Adsorption of a Bottlebrush Polymer in Nanopores

Panagiotis Kardasis, Ioannis Tzourtzouklis, Yun Dong, Moritz Meier-Merziger, Hans-Jürgen Butt, Holger Frey, and George Floudas*

Read Online

ACCESS | Metrics & More | Article Recommendations | SI Supporting Information

ABSTRACT: We report on the imbibition kinetics of bottlebrush polymer *cis*-1,4-polyfarnesene (PF) during flow in nanopores. To follow the polymer flow *in situ*, we employ *in situ* nanodielectric spectroscopy. The technique provides simultaneous access to the kinetics of imbibition and to the molecular dynamics during flow on the segmental and chain length scales. The imbibition process follows the $t^{1/2}$ dependence as predicted by the Lucas–Washburn equation. However, bottlebrush polymers with a molecular size smaller than the pore diameter ($2R_g < d$, d is the pore diameter) penetrate nanopores with a higher effective viscosity than in bulk. The adsorption time scales are much longer than any molecular process, being several orders of magnitude slower than the segmental and longest normal modes. Compared to linear polymers, bottlebrush polymers exhibit even slower adsorption with characteristic time scales having a weak molar mass ($\tau_{ads} \sim N_{bb}^{1.2 \pm 0.1}$, N_{bb} is the number of backbone repeat units), pore size ($\log(\tau_{ads}) \sim \xi/d$, $\xi = 20$ nm), and temperature ($E_{act} \sim 16 \pm 2$ kJ/mol) dependence. These findings are discussed in terms of an increased number of contacts of the bottlebrush polymer with the surface. Lastly, we investigate the separation of a polymer blend with linear/bottlebrush topologies into its constituents by the difference in the imbibition kinetics.
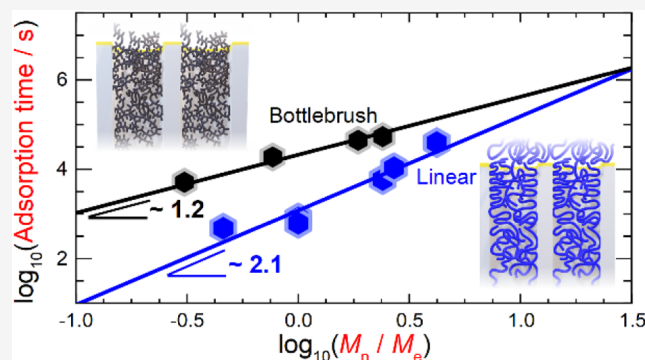
1. INTRODUCTION

The formation of polymer layers next to an interface by the adsorption of chains is a largely irreversible process associated with several technological applications: from adhesion, and lubrication, to colloidal stabilization.[1−4] Within the adsorbed layers, chains adopt different configurations, *e.g.*, loops, trains, and tails. Polymer topology can strongly affect the type of configurations. For example, ring polymers can form only form loops. Star polymers with their large number of chain ends per macromolecule can have an increased number of tails. Branched or comb polymers, also known as bottlebrushes,[5] have an even higher number of chain ends that are expected to affect the chain configurations within the adsorbed layer. Bottlebrushes, depending on the strength of polymer–substrate interactions, as well as the chemical identity of the backbone and side chains, can form strongly adsorbed to weakly adsorbed chains.[6−8] In the former case, side chains assume quasi-two-dimensional (2D) configurations, whereas in the latter, the configurations resemble more three-dimensional (3D). Despite the current interest in bottlebrush polymers with respect to a wide range of applications (as supersoft elastomers and smart, soft/elastic surfaces), little is known about the way that bottlebrushes adsorb on surfaces.

The flow of polymers through nanochannels (a process known as polymer imbibition) and the way the chains are interacting with the pore walls is another related area with applications ranging from inkjet printing,[9] lab-on-a-chip systems,[10] and polymer mixture separation[11,12] to oil recovery.[13] When polymers flow in nanochannels having a diameter significantly exceeding the polymer size, polymer adsorption takes place resulting in immobilized chains at the pore walls, forming a "dead zone".[14] There is significant progress in understanding the way that polymer chains penetrate nanopores, for linear and star-shaped topologies, by experiment,[11,12,15−25] theory,[14,26,27] and simulation.[28−34] However, studies on the imbibition of bottlebrush polymers in nanopores do not exist, to the best of our knowledge.

Herein, we report on the effect of polymer topology on adsorption kinetics during imbibition in nanopores. For this purpose, we employ a series of bottlebrush *cis*-1,4-polyfarnesenes (PF)[35−37] (comprising short side chains). We explore the role of the side chains in imbibition and adsorption kinetics in comparison to the linear *cis*-1,4-polyisoprenes (PI). To this end, we employ nanodielectric spectroscopy (*n*DS).[16,20] The technique provides simultaneous access to the kinetics of
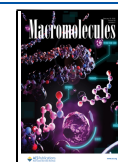
Table 1. Molecular Characteristics of *cis*-1,4-Polyisoprene (PI), *cis*-1,4-Polyfarnesene (PF), and Their Binary Mixtures

sample	N_{bb}	M_n (kg·mol^{-1})[a]	$Đ$[b]	1,4 [%][c]	3,4 [%][c]	$\eta_{0@303K}$ (Pa·s)[d]	R_g (nm)
PI-10	141	9.6	1.04	94.7	5.3	12	3.09[e]
PI-18	268	18.3	1.04	94.1	5.9	28	4.26[e]
PI−25	359	25.0	1.02	94.5	5.5	65	4.98[e]
PI−38	564	38.4	1.01	94.7	5.3	434	6.18[e]
PI−50	770	50.0	1.05	93.0	7.0	1626	7.05[e]
PF−4	18	3.6	1.11	93.0	7.0	0.8	1.30[f]
PF−9	43	8.8	1.14	93.1	6.9	2.6	2.03[f]
PF−15	75	15.4	1.11	93.5	6.5	8	2.68[f]
PF−38	188	38.4	1.07	93.5	6.5	28	4.23[f]
PF−93	455	93.0	1.06	93.4	6.6	80	6.59[f]
PF−120	590	120.6	1.07	94.0	6.0	182	7.50[f]
PF−212	929	211.9	1.09	93.6	6.4	877	9.94[f]
PF−342	1674	342.1	1.21	93.0	7.0	4990	12.64[f]
PF−592	2895	591.7	1.20	94.4	5.6	28,540	16.62[f]
PF−high 3,4	377	77.0[b]	1.1	61.0	39.0	-	5.99[f]

Blends			
sample	Z_{PF}/Z_{PI}[g]	blend composition (wt %)	$\eta_{0@303K}$ (Pa·s)[d]
PF-4/PI-38	0.07/8	50/50	25
PF-15/PI-50	0.30/10	50/50	308
PF-120/PI-10	2.4/2	50/50	50
PF-120/PI-18	2.4/4	50/50	104
PF-120/PI-25	2.4/5	50/50	130

[a]M_n calculated from M_w (MALS) and $Đ$ values. [b]Determined by SEC using a PI calibration and THF as eluent. [c]Determined via ^{1}H NMR spectroscopy. [d]Zero-shear viscosity measured at T = 303 K. [e]Radius of gyration of the polyisoprene chain calculated as[41] $R_g^{(chain)} = \sqrt{\frac{\langle R_0^2 \rangle}{6}}$ with $\frac{\langle R_0^2 \rangle}{M_n} = \frac{a_{tube}^2}{M_e} = 5.96 \frac{nm^2}{kg/mol}$, where M_n is the molar mass, M_e is the entanglement molar mass, and a_{tube}, is the tube diameter. The values were obtained from ref 41.[41] [f]Radius of gyration of the PF evaluated as $R_g = \sqrt{\frac{\langle R_0^2 \rangle}{6}}$, where the $\langle R_0^2 \rangle$ was estimated by two different but equivalent methods. See the Experimental Section for details. [g]Ratio of number of entanglements.

imbibition and to the molecular dynamics during flow at the segmental and chain length scales. We employ anodic nanoporous aluminum oxide (abbreviation: AAO) templates that are sputtered with a thin gold layer to transform the membranes into capacitors. A polymer melt on the top surface of a template penetrates the pores by capillary action. By recording the evolution of capacitance, C, upon an ac-field, it is possible to extract the complex dielectric function ($C^* \sim \varepsilon^*$), where the details of the polymer dynamics during flow (*e.g.*, *in situ*) are encoded. Our objective of this study is to determine the scaling laws for the imbibition and adsorption times of bottlebrush polymers as a function of molar mass, pore size, and temperature in comparison to other topologies.

We demonstrate that the bottlebrush topology results in slower adsorption in nanopores in comparison to linear PIs albeit with a different molar mass dependence. Additionally, the characteristic adsorption times for PFs present a weaker pore and temperature dependence when compared with both linear and star polymers. The weaker temperature dependence of the adsorption times is discussed in terms of polymer configurations at the pore walls and an increasing number of contacts with the surface. Lastly, we explore how symmetric PF/PI blends penetrate the same nanopores. We show that differences in the imbibition and adsorption kinetics of the two topologies can be used to separate a homogeneous bottle-brush-linear (PF/PI) blend from its components. Based on this finding, we can propose this as a separation method (like GPC) for homogeneous polymer blends but in the absence of solvent (unlike GPC).

2. EXPERIMENTAL SECTION

2.1. Samples, Synthesis, and Molecular Characteristics. All polyfarnesene samples were prepared via carbanionic polymerization using a high vacuum technique. The absence of any termination and transfer reaction facilitates a controlled polymerization that offers the precise adjustment of the molar mass by the relationship of the molar mass of the monomer unit (M_0) and the ratio of the monomer and initiator concentration ($[M]_0/[I]$): $M_n = M_0 \cdot [M]_0/[I]$. Polymerizations were performed in *n*-heptane and under an inert argon atmosphere using *sec*-butyl lithium (*sec*-BuLi) as the initiator. A detailed description of the synthesis and characterization of all 1,4-PF samples was recently published elsewhere.[37] To alter the resulting microstructure of the polydiene, the polarity of the solvent can be changed. For this reason, methyl *tert*-butyl ether (MTBE) was used to enhance the 3,4-incorporation.[38] The polymerization was performed according to the previously reported procedure, and MTBE was dried accordingly, using *sec*-BuLi and diphenylethylene.[37,38] Using MTBE as neat polymerization medium gives 61.0% 1,4-incorporation, 38.7% 3,4-PF, and 0.3% 1,2-PF as determined via ^{1}H NMR, see Figure S3, Supporting Information.[38,39] All polyisoprene samples were purchased from PSS Polymer Standards, Mainz, Germany. The respective size exclusion chromatography (SEC) traces of all synthesized polymer samples are given in the Supporting Information; see Figures S1 and S2.

Both PI and PF are typical type-A polymers, according to Stockmayer,[40] meaning that they have a component of dipole moment along the backbone. This allows for a study of both the segmental and chain dynamics using dielectric spectroscopy. From a topological point of view, in comparison to polyisoprene, polyfarnesene has two isoprene repeats as side group ($m_{PF}^0 \sim 3m_{PI}^0$, where m^0 is the molar mass of a repeat unit). As a result, the PF bears also two components of the dipole moment (one vertical and one parallel

to the polymer backbone). Moreover, a recent study revealed that by increasing the size of side group, the tube diameter and packing length increase (chain thickening).[36] In addition, the viscoelastic properties of PF differ substantially compared to PI. The plateau modulus decreases approximately by an order of magnitude, the glass-to-liquid temperature decreases by ~8 K and the entanglement molar mass is M_e^{PF}(=50 kg/mol) e.g. 10 M_e^{PI}.[35−37] To compare the size of PF to the pore diameter, the characteristic mean-square end-to-end distance of PF was, initially, evaluated as $\langle R_0^2 \rangle / M_n = a_{tube}^2 / M_e = 2.8 \frac{nm^2}{kg / mol}$, where M_n is the molar mass, M_e is the entanglement molar mass, and α_{tube} = 11.8 nm is the tube diameter.[41] Polyfarnesene resembles densely grafted bottlebrushes as a result of the high grafting density (z = 1 side chain per monomer). In addition to the estimated end-to-end distance the diagram of states, by Paturej et al.,[5] provides another estimate: $\langle R_0^2 \rangle^{1/2} = (v_0 l_m z N_{sc})^{1/4} N_{bb}^{1/2} = 0.75$ nm $N_{bb}^{1/2}$, where v_0(=0.3764 nm³) is the monomer volume, l_m(=0.42 nm) is the monomer length, N_{sc}(=2) is the number of repeated units in the side chain, and N_{bb} is the number of repeat units in the backbone. Both models give the same value. This shows a clear impact of N_{sc} on the tube diameter, a_{tube}, and packing length, p, respectively, as $a_{tube} = (v_0 l_m z N_{sc})^{1/4} (N_e)^{1/2}$ and $p = \left(\frac{v_0}{l_m z N_{sc}} \right)^{1/2}$. These predictions, at least for the PF, are in excellent agreement with the experimental results. Moreover, the bottlebrush thickness is denoted as $2 \times \langle R_{sc}^2 \rangle^{1/2} = 2 \left(\frac{v_0 z}{l_m} \right)^{1/2} N_{sc}^{1/2} \sim 2.7$ nm, where $\langle R_{sc}^2 \rangle$ is the mean square size of side chains.

In addition to the homopolymers, a series of symmetric blends (PF-M_n/PI-M_n) was used in this study. The summary of all of the samples and their molecular characteristics are provided in Table 1.

2.2. Rheology. The viscoelastic properties of the homopolymers (PIs and PFs) as well as of their blends were measured with an AR-G2 rheometer (TA Instruments), with a magnetic bearing that allows low nanotorque control. The samples were prepared on the lower plate of an 8 mm diameter parallel plate geometry. For the lower molar mass PFs, plates of 20 and 40 mm in diameter were also employed. Isothermal frequency scans were used to record the storage (G') and loss (G'') moduli in the angular frequency range (ω) from 0.1 to 100 rad·s⁻¹ and for several temperatures. Temperature control was made with an environmental chamber, in the range from 193 to 343 K. The time−temperature superposition (tTs) principle, allows the frequency dependence of the complex modulus, G^*, at any temperature to be determined from a master curve at a reference temperature, T_{ref}, as $G^*(\omega,T) = b_T G^*(a_T \omega, T_{ref})$, where a_T and b_T are frequency-scale and modulus-scale shift factors, respectively. The viscosities were calculated according to the relation $\eta^* = \frac{G^*}{\omega}$ and the zero-shear viscosities at T_{ref} as $\eta_0 = \lim_{\omega \to 0} |\eta^*| \sim \frac{G''}{\omega}$. The zero-shear viscosities of the homopolymers are shown as a function of temperature in Figures S4 and S5, in the Supporting Information, and the Vogel−Fulcher−Tammann (VFT) parameters of the zero-shear viscosity ($\log_{10}(\eta_0) = \log_{10}(\eta_\infty) + \frac{B}{T - T_0}$, where η_∞ is the zero-shear viscosity in the limit of high temperatures, B is the activation parameter, and T_0 is the "ideal" glass temperature) are included in Table S1. The values of the zero-shear viscosities at T = 303 K (imbibition temperature) are included in Table 1 in the main text for both the homopolymers and the blends.

2.3. Dielectric Spectroscopy (DS). The dynamics of the PI and PF homopolymers in bulk and their binary mixtures were studied by dielectric spectroscopy.[42] Measurements were carried out as a function of temperature (in the range from 193 to 333 K) and frequency (in the range from 10⁻² to 10⁶ Hz), with a Novocontrol α frequency analyzer composed of a broadband dielectric converter and an active sample hand. The usual parallel plate geometry of silver electrodes was employed. The electrodes were 20 mm in diameter and the space between them was maintained by Teflon spacers of 50 μm in thickness. The complex dielectric function $\varepsilon^*(\omega,T) = \varepsilon'(\omega,T)$

$- i\varepsilon''(\omega,T)$, where ε' is the real part and ε'' is the imaginary part (dielectric losses), was recorded as a function of frequency, f ($=\omega/2\pi$), and temperature, T. The complex dielectric function is also given as a superposition of Debye functions with different characteristic relaxation times, τ, as

$$\varepsilon^*(\omega, T) = \varepsilon' - i\varepsilon'' = \varepsilon_\infty + \int_{-\infty}^{+\infty} \frac{\Delta\varepsilon \cdot g(\tau)}{1 + i\omega\tau} d(\ln(\tau)) \text{and}$$
$$\int_{-\infty}^{+\infty} g(\tau) d(\ln(\tau)) = 1 \tag{1}$$

with $\omega = 2\pi f = \tau^{-1}$, $\Delta\varepsilon = \varepsilon'_s - \varepsilon_\infty$ is the dielectric strength (ε'_s is the static dielectric permittivity and ε_∞ is the permittivity in the limit of very high frequencies), and $g(\ln(\tau))$ the distribution of relaxation times. The measured complex dielectric data as a function of frequency and for a given temperature, can be fitted by the empirical equation of Havriliak and Negami:[42]

$$\varepsilon^*(\omega, T) = \varepsilon' - i\varepsilon''$$
$$= \varepsilon_\infty + \sum_k \frac{\Delta\varepsilon_k(T)}{[1 + (i \cdot \omega \cdot \tau_{HN,k}(T))^{m_k}]^{n_k}} + \frac{\sigma_0(T)}{i\varepsilon_0\omega} \tag{2}$$

where $\Delta\varepsilon_k$ is the dielectric strength, $\tau_{HN,k}$ is the H−N characteristic relaxation time and the index k indicates the process under investigation. The uprise at lower frequencies is due to conductivity contributions as $\sigma_0/\varepsilon_0\omega$, where σ_0 is the dc-conductivity and ε_0 (= 8.854 × 10⁻¹² F m⁻¹) is the permittivity of free space. The parameters m_k and n_k (0 < m_k, $m_k n_k \leq 1$) provide the symmetric (low-frequency slope) and asymmetric (high-frequency slope) broadening of the distribution of relaxation times, respectively. The characteristic frequency at maximum loss ($f_{max} = 1/2\pi\tau_{max}$, where τ_{max} is the characteristic relaxation time) are presented herein and have been analytically obtained from the Havriliak−Negami equation as follows:

$$\tau_{max,k} = 1/2\pi f_{max,k}$$
$$= \tau_{HN,k} \left[\sin\left(\frac{\pi m_k n_k}{2(1 + n_k)} \right) / \sin\left(\frac{\pi m_k}{2(1 + n_k)} \right) \right]^{1/m_k} \tag{3}$$

2.4. In Situ Nanodielectric Spectroscopy (nDS). To follow the imbibition and adsorption kinetics of the homopolymers (PIs and PFs) and their symmetric blends into the nanopores, we employed in situ nanodielectric spectroscopy (nDS).[11,15−19] A schematic representation of the setup is presented in Figure 1. The setup consists of an anodic alumina oxide (AAO) template of which the top and bottom sides are sputtered with a thin layer of gold (~30 nm). The gold layers served as the electrodes. Native AAO templates with open ends in both sides, a well-defined pore diameter, d, (= 100 nm, 40 or 20 nm) and a thickness of L = 100 μm were purchased from InRedox (Longmont, VA). The corresponding porosities were 24 ± 3% (at d = 100 nm), 12 ± 2% (at d = 40 nm), and 11 ± 2% (at d = 20 nm) as obtained by SEM (Figure S6, Supporting Information). Before the infiltration process, all AAO templates were annealed in a vacuum oven at a temperature of 185 °C for at least 12 h. This annealing step eliminates the majority of hydroxyl (−OH) groups from the surface of the AAO. Earlier studies of water and alcohol crystallization within the same nanopores have shown that the inner surface is smooth and cannot induce heterogeneous nucleation.[43,44] Additional SEM images from cross sections of the AAO templates are provided in Figure S7 and the Supporting Information. In general, they depict a uniform pore length.

In situ dielectric measurements were performed at constant temperatures, at ambient pressure, and for frequencies in the range of 10−10⁶ Hz, e.g., over a narrower frequency range as compared to usual DS. Polymer infiltration (imbibition) was made by placing a drop of the sample on top of AAO templates. The molecular mass of the polymer as well as the temperature and frequency ranges are chosen judiciously, so as the longest normal mode(s) to appear within the frequency window. With this frequency range, the time required for a single dielectric curve is from 0.5 to 2.5 min. Subsequently,
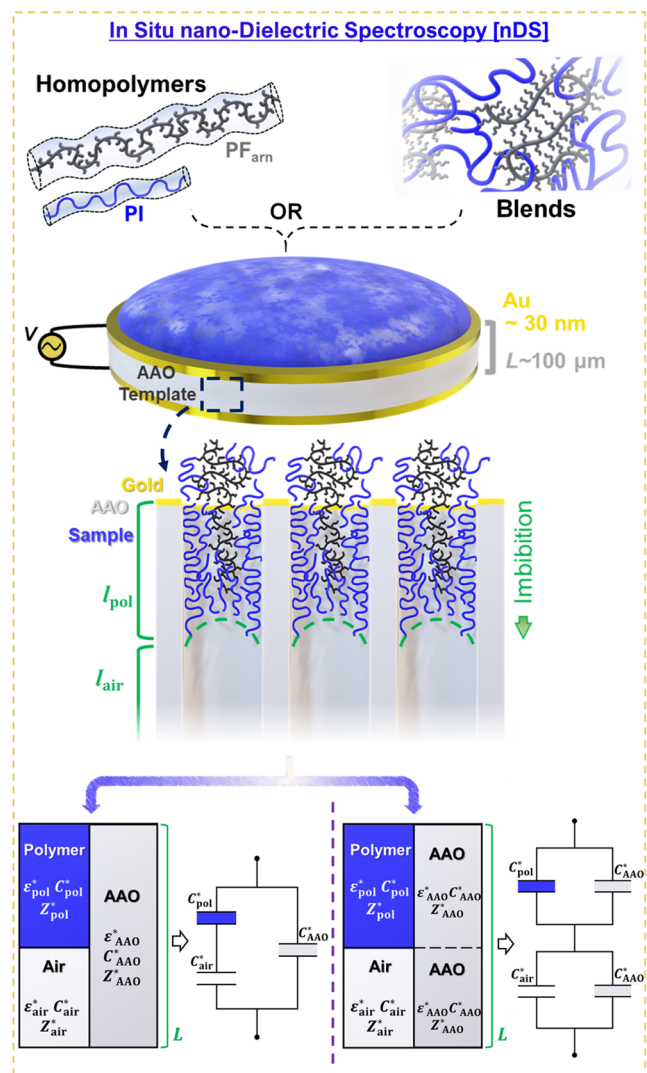
Figure 1. Schematic representation of the nanodielectric spectroscopy setup (top) and equivalent geometry (bottom) employed for the *in situ* imbibition of the homopolymers (PI & PF) and their PF/PI blends. A thin layer of gold on the top and bottom of the AAO template served as an electrode. A droplet of the sample was placed on top of the template. The total dielectric response was measured continuously as a function of time and frequency by applying an ac electric field.

during prolonged annealing, the evolution of the dielectric loss curves for the longest chain mode (known as the normal mode, NM) are recorded. We should note that at the imbibition temperature, the segmental process is out of our experimental window. At high frequencies, an upturn of dielectric losses, ε'', is evident due to the background signal (induced from the Au-sputtered electrodes). The contribution from effects related to ion mobility, such as electrode polarization, will only appear at much lower frequencies than the range of interest (*e.g.*, the normal modes). As with normal DS measurements, the Quatro Cryosystem (by Nocontrol) was used for temperature stabilization within the cryostat (temperature stability of 0.01 K).

For the *in situ* measurements, the total capacitance can be discussed by two different circuits (Figure 1).[15,17,19] In the case of the 3-capacitors, the equivalent circuit is $C_{tot}^* = [1/C_{pol}^* + 1/C_{air}^*]^{-1} + C_{AAO}^*$, where C_{tot}^* refers to the total capacitance, C_{pol}^* to the capacitance of polymer within the pores, C_{air} to the remained air within the pores, and C_{AAO}^* to the contribution of the bare alumina. The individual capacitance is $C_i^* = \varepsilon_i^* A / l_i$, where l_i is the capacitor thickness and A is

the area of the electrode. Thus, the total dielectric function is given by $\varepsilon_{tot}^* = \frac{\phi \varepsilon_{pol}^*}{\lambda + (1 - \lambda)\varepsilon_{pol}^*} + \varepsilon_{AAO}^*(1 - \phi)$. Here, $\lambda \equiv l_{pol}/L$ ($0 \leq \lambda \leq 1$) is the penetrated length, ϕ ($= V_{pores}/V_{tot}$) is the porosity, and ϕ_{AAO} is the fraction of alumina. Alternatively, given the strongly anisotropic length-to-diameter ratio of the nanopores, one may assume an equal potential along the imbibition front line. In this case, the equivalent circuit is composed of four capacitors. The comparison between the two different capacitor models is provided elsewhere.[19] In the latter model the total capacitance is given by $C_{tot}^* = [(C_{pol}^* + C_{AAO}^*)^{-1} + (C_{air}^* + C_{AAO}^*)^{-1}]^{-1}$ and equivalently, the total dielectric function can be obtained as

$$\varepsilon_{tot}^* = \varepsilon_{tot}' - i\varepsilon_{tot}'' = \frac{A_1 B_1 + A_2 B_2}{B_1^2 + B_2^2} - i\frac{A_2 B_1 - A_1 B_2}{B_1^2 + B_2^2}$$

$$A_1 = \phi^2 \varepsilon_{pol}' + \phi(1 - \phi)[\varepsilon_{AAO}'(\varepsilon_{pol}' + 1) - \varepsilon_{pol}''\varepsilon_{AAO}''] + (1 - \phi)^2 [\varepsilon_{AAO}'^2 + \varepsilon_{AAO}''^2]$$

$$A_2 = \phi^2 \varepsilon_{pol}'' + \phi(1 - \phi)[\varepsilon_{AAO}''(\varepsilon_{pol}' + 1) + \varepsilon_{pol}''\varepsilon_{AAO}'] + (1 - \phi)^2 [2\varepsilon_{AAO}'\varepsilon_{AAO}'']$$

$$B_1 = \phi[\varepsilon_{pol}' - \lambda(\varepsilon_{pol}' - 1)] + (1 - \phi)\varepsilon_{AAO}'$$

$$B_2 = \phi(1 - \lambda)\varepsilon_{pol}'' + (1 - \phi)\varepsilon_{AAO}''$$

$$\lambda \equiv l_{pol}/L$$

$$\phi = 1 - \phi_{AAO} \tag{4}$$

The dielectric response of the AAO templates was extracted by measuring the empty templates, as

$$\varepsilon_{empty}^* = \varepsilon_{empty}' - i\varepsilon_{empty}'' = \varepsilon_{AAO}^*(1 - \phi) + \varepsilon_{air}^*\phi \tag{5}$$

Considering that $\varepsilon_{air}^* = 1$, the imaginary part of the alumina (losses) translates vertically to the ε_{tot}^* curves, we can simplify the total dielectric function by subtracting the empty cell signal (assuming a minimum contribution to the dielectric losses from the alumina $\varepsilon_{AAO}'' \approx 0$).[15,17,19] Notably, there is no effect of air on the relaxation times for both models, and this is because of the low polarity of the polymer.[19] Thus, the final expression for the total dielectric losses during imbibition ($l_{pol} < L$ or $\lambda < 1$) in the 4-capacitor model is

$$\varepsilon_{tot}'' = \frac{\varepsilon_{pol}''\lambda\phi[2\phi(1 - \phi)\varepsilon_{AAO}' + (1 - \phi)^2\varepsilon_{AAO}'^2 + \phi^2]}{[\lambda\phi + (1 - \phi)\varepsilon_{AAO}' + (1 - \lambda)\phi\varepsilon_{pol}']^2 + \phi^2(1 - \lambda)^2\varepsilon_{pol}''^2}$$

$$= \varepsilon_{pol}''\phi \frac{\lambda\varepsilon_{empty}'^2}{[\varepsilon_{empty}' + \phi(1 - \lambda)(\varepsilon_{pol}' - 1)]^2 + \phi^2(1 - \lambda)^2\varepsilon_{pol}''^2} \tag{6}$$

The two models differ on the growth of ε_{tot}'' as a function of imbibition time or $\lambda(t)$, especially for templates of high porosity. In the 3-capacitors model, the growth of $\varepsilon_{tot}''(t)$ with λ is a parabola, whereas in the 4-capacitors model is roughly linear. Hence, the latter model is closer to the linear growth of $\lambda(t)$ found experimentally. For fully infiltrated nanopores ($\lambda = 1$), the measured total capacitance is given by $C_{tot}^* = C_{pol}^* + C_{AAO}^*$. Hence, there is a simple relation of the measured total complex dielectric function, given by

$$\varepsilon_{pol}^* = \frac{\varepsilon_{tot}^* - (1 - \phi)\varepsilon_{AAO}^*}{\phi} \tag{7}$$

3. RESULTS AND DISCUSSION

3.1. PF Dynamics in Bulk. The viscoelastic behavior of PF for a wide range of molar masses is discussed with the help of Figure 2a. Polyfarnesene exhibits the typical rheological features of amorphous linear polymers. The master curves for the storage (G') and loss (G'') shear moduli were produced
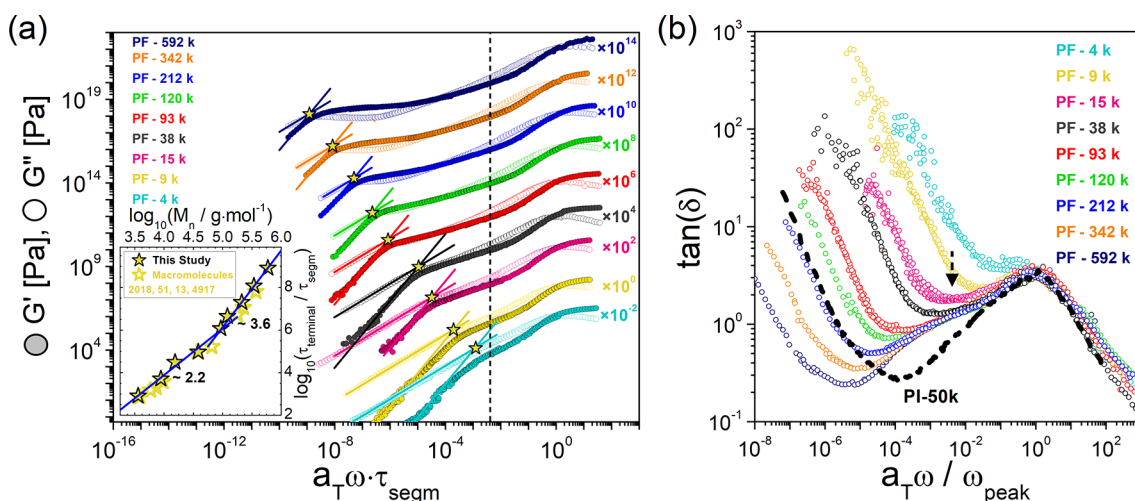
Figure 2. (a) Comparison of the rheological curves of PF for different molar masses. Master curves of the frequency-dependent storage (G') and loss (G'') moduli are shown with filled and empty symbols, respectively. The curves are normalized to the segmental relaxation time and, furthermore, vertically translated for clarity. Lines with respective slopes of 2 and 1 are used to obtain the terminal (flow) characteristic frequency (yellow star symbols). In the inset, the characteristic relaxation times corresponding to the terminal relaxation reduced to that of the segmental are presented and compared with data from the literature.[35] Lines with slopes of ~2.2 and 3.6 are indicated. (b) Respective $\tan(\delta) = G''/G'$ normalized to the peak of the segmental relaxation. The black dashed line corresponds to PI-50 ($M_n \sim 10\ M_e$) and is shown for comparison.
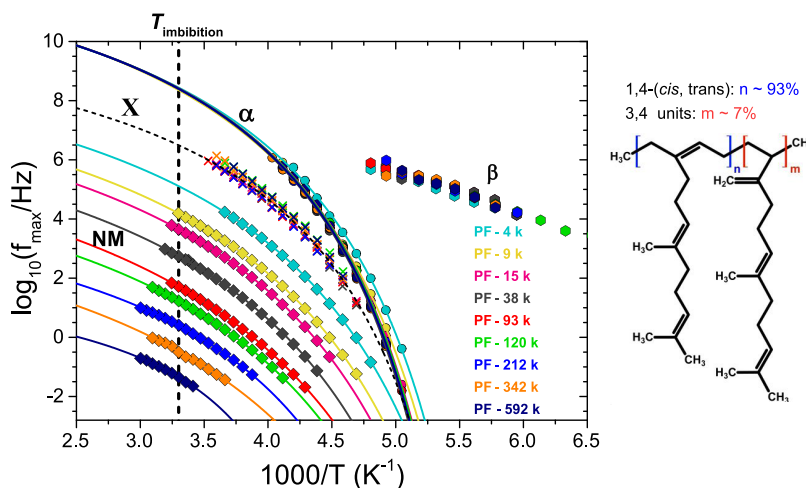
Figure 3. (Left) Characteristic frequencies at maximum loss as a function of inverse temperature for the bulk PF; β-process (hexagons), segmental α-process (circles), X-process (crosses), and longest normal mode (NM) process (rhombi) for different molar masses depicted with different colors. The curved lines represent fits to the VFT equation. (Right) Schematic of polyfarnesene microstructure.

by employing the principle of time−temperature superposition (tTs) and are further normalized to the characteristic segmental time (τ_{segm}). Four regimes can be identified, from higher to lower frequencies: (i) the glassy, (ii) the transition region between the two crossovers of $G'(\omega)$ and $G''(\omega)$, (iii) the rubbery plateau for higher molar masses ($M_e \sim 50$ kg/mol), and (iv) the typical terminal region ($G'(\omega) \approx \omega^2$ and $G''(\omega) \approx \omega^1$). The dependence of the terminal time on molar mass is shown in the inset of Figure 2a together with literature data. They have a slope of 2.2 and 3.6, for the lower ($M_n < M_e$) and higher molar masses ($M_n > M_e$), respectively. A change in the slope of $G'(\omega)$ (in the transition region) is evident, indicating another process roughly 2 orders of magnitude slower than the segmental process (vertical black dashed line in Figure 2a). This process can be clearly seen in the $\tan(\delta) = G''/G'$ representation in Figure 2b, identified as a shoulder at lower frequencies as compared to the segmental process (peak). The respective data for a PI-50 are shown for

comparison. This is a characteristic molecular process independent of the backbone length and can be also observed in PMyr (polymyrcene)[36] (one repeat unit in the side group) in Figure S8, Supporting Information. This intermediate process has two origins. One associated with sub-Rouse dynamics of a unit longer than the segment length but smaller than an entanglement strand.[45] Another origin can be the contribution from the slower-segmental process of the 3,4-units (~7%).

To clarify the origin of the intermediate process, we employed DS. The dielectric loss curves of PF-93 are presented in Figure S9, in the Supporting Information. An intermediate process denoted as X-process, is evident in the dielectric loss curves, as a shoulder of the segmental process. The analysis is supported by a model-free evaluation of the distribution of relaxation times (based on the Tikhonov algorithm). The comparison of dielectric loss curves of PF-342 and PI-38 ($M_n/M_e \sim 8$) together with the distribution of

relaxation times are shown in Figure S10. Notice that the algorithm provides not only the exact position of the longest normal mode but also the internal Rouse modes.

In general, the longest normal mode of PF has significantly lower dielectric strength than that of PI. The temperature dependence of all processes for a range of molar masses is shown in Figure 3 together with a schematic of the PF microstructure. Starting from lower temperatures, a fast and local β process is shown with an Arrhenius temperature dependence, $f_{max} = f_\infty \exp(-E/RT)$, where f_{max} is the frequency at maximum loss, f_∞ the frequency at very high temperatures, E (= 28 ± 2 kJ/mol) is the apparent activation energy, and R is the gas constant. The different activation energy with respect to linear PI chains could reflect the different 3,4 unit content in the two topologies (Table 2). At higher temperatures, three

Table 2. Characteristic Activation Energies for the Adsorption, Segmental, and Local β-Process of the Three Different Architectures and the Polymer-Surface Number of Contacts ($N*$)

| topology	$E_{act.}^{ads.}$ [kJ/mol]	$E_{act.@303K}^{segm.}$ [kJ/mol]	$E_{act.}^{\beta}$ [kJ/mol]	$N*$
linear	71 ± 4	52 ± 2	41 ± 2	9
star ($f = 6$)	61 ± 2	53 ± 2	41 ± 2	15
star ($f = 64$)	45 ± 6	53 ± 2	41 ± 2	49
bottlebrush	16 ± 2	45 ± 2	28 ± 2	56

processes are evident: the segmental α-process (associated with the liquid-to-glass temperature), the X-process, and the longest normal mode. The latter depends on molar mass, whereas the X-process is unaffected by the M_n. All three processes conform to a Vogel−Fulcher−Tammann (VFT) temperature dependence[42] according to $f_{max} = f_\infty \exp(-B/(T - T_0))$, where B is the activation parameter and T_0 is the "ideal" glass temperature. Comparison of the relaxation map of PF-93 as obtained from rheological and dielectric measurements is presented in Figure S11, Supporting Information. The X-process in rheology is quite broad, and this induces a large systematic error in the extracted relaxation frequencies. On the other hand, the dielectric relaxation data avoid any application of a time−temperature superposition; hence, the extracted characteristic frequencies are more accurate.

To elaborate further on the origin of the X-process, a PF homopolymer with a higher 3,4-content was synthesized and investigated by DS. A comparison of the dielectric loss curves and their distribution of relaxation times is shown in Figure S12. The proximity of the X-process in the dielectric loss curve of cis-1,4-PF to the main α-process of 3,4-PF suggests its origin (as reflecting contributions from the slow 3,4-units). Other possible contributions include the sub-Rouse modes mentioned above[45] and subchain relaxation reported earlier in confined PI.[46]

The respective master curves obtained from rheology and the tan(δ) = G''/G' are shown in Figure S10.

3.2. PF Kinetics during Imbibition in Nanopores.
Here we discuss the adsorption kinetics of polyfarnesene following the full imbibition by employing in situ nDS. The technique provides simultaneous access to the kinetics of imbibition and to the dynamics at the length scale of normal modes (dielectric strength, distribution of relaxation times, and average relaxation times). The results are compared to the respective linear and star-shaped PIs, with the aim to understand the effect of chain topology on the adsorption process.[17,19] The

imbibition and adsorption kinetics are monitored by following the changes in the dielectric loss curves of the normal modes as a function of time. Figure 4a depicts the evolution of the
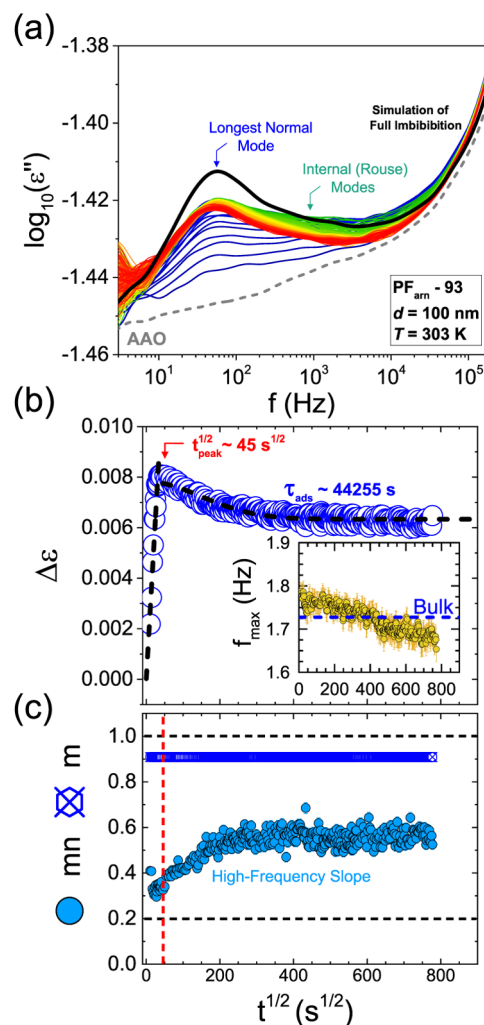
Figure 4. (a) Evolution of dielectric loss curves for PF-93 during imbibition (blue curves) and adsorption (from green to red curves) within an AAO template with a pore diameter of 100 nm and at 303 K ($\sim T_g$ + 100 K). The peak corresponds to the longest normal mode. The gray dashed curve corresponds to the signal of the measured empty template (background). The black thick line is the expected signal at complete imbibition based on eq 7. (b) Evolution of the dielectric strength, $\Delta\varepsilon$, as a function of the square root of time. Dashed lines represent fits (see text) to the two mechanisms (imbibition vs adsorption). The inset shows the characteristic frequency at maximum loss as a function of square root of the annealing time. The blue dashed line gives the corresponding value in the bulk. (c) Evolution of the characteristic parameters of the distribution of relaxation times for the longest normal mode. A drastic change of the high-frequency slope (mn) is evident following the full imbibition.

dielectric loss curves during and following the full imbibition of PF-93 into AAO nanopores having pores with a diameter of 100 nm at a temperature of 303.15 K (located about 100 K above the T_g). The peak, in Figure 4a, corresponds to the longest normal mode, whereas the segmental process is out of the experimental window (e.g., is faster). The expected dielectric loss curve, ε''_{tot} corresponding to full imbibition (from eq 7), based on the measured ε''_{pol} (in bulk), as well as

the bare ε''_{AAO} is shown in Figure 4a for comparison with the black line.

By fitting each dielectric loss curve to a summation of two Havriliak—Negami functions, the evolution of the dielectric strength of the longest normal mode, $\Delta\varepsilon(t)$, was extracted and plotted in Figure 4b as a function of $t^{1/2}$. Initially, the increasing $\Delta\varepsilon(t)$ scales linearly with $t^{1/2}$ as anticipated from the proportionality of $\Delta\varepsilon(t) \sim l_{\text{pol}}(t)$, where $l_{\text{pol.}}$ is the infiltrated length of the polymer within the channel. According to Lucas—Washburn equation (LWE),[28,47,48] the time dependence of $l_{\text{pol}}(t)$ is given as

$$l_{\text{pol}}(t) = \left(\frac{\gamma\, R_{\text{p}}\, \cos\theta}{2\eta_0} \right)^{1/2} t^{1/2}$$

$$(8)$$

where γ (=30.1 mN/m)[23] is the surface tension, θ (cos θ = 0.88) is the advancing contact angle, R_{p} is the pore radius, and η_0 is the zero-shear viscosity. The predicted full-infiltration (wetting) time, denoted here as $t_{\text{L−W}}$, can be estimated based on the LWE equation at $l_{\text{pol}} = L = 100\ \mu\text{m}$. Following the linear increase in $\Delta\varepsilon(t)$, there is a subsequent slow decrease that reflects the adsorption of chains at the pore walls. From the evolution of the $\Delta\varepsilon(t)$, we can extract two characteristic time scales; t_{peak} or $\tau_{\text{imbibition}}$ corresponding to the time of the complete filling of nanopores, and the characteristic adsorption time, τ_{ads}. The latter is obtained by fitting the data to an exponential decay function. The respective dependencies of the dielectric strength during imbibition and adsorption are fitted as $\Delta\varepsilon = a + \beta\sqrt{t}$, $t < t_{\text{peak}}$, and $\frac{\Delta\varepsilon - \Delta\varepsilon_{\text{min}}}{\Delta\varepsilon_{\text{max}} - \Delta\varepsilon_{\text{min}}} = \exp\left(\frac{t - t_{\text{peak}}}{\tau_{\text{ads}}} \right)$, $t > t_{\text{peak}}$. Here, $\Delta\varepsilon_{\text{min}}$ refers to background subtraction.

The dielectric strength of the longest normal mode (NM) is given by $\Delta\varepsilon_{\text{NM}} = \frac{4\pi n_{\text{p}}\mu_\parallel^2}{3k_{\text{B}}T}\langle r^2 \rangle$, where n_{p} (=$\rho N_{\text{A}}/M_w$, ρ is the mass density, and M_{w} is the weight-average molar mass) is the number density of chains, $\mu_\parallel^2$ is the electric dipole moment per contour length, and $\langle r^2 \rangle$ is the mean end-to-end distance of the chain. Once a chain is partially or completely anchored on the surface (pore walls), it becomes partially or completely unable to fluctuate in time and space and hence becomes dielectrically inactive and $\Delta\varepsilon$ decreases. In the case of PF-93, shown in Figure 4b, the characteristic adsorption time, τ_{ads}, was evaluated to the order of roughly half a day ($\tau_{\text{ads}} \sim 44260$ s). In the inset of Figure 4b, we present the evolution of f_{max} for the longest normal mode. At the final stages, f_{max} is lower than the respective value in the bulk, revealing slower dynamics for the longest normal mode. As we will discuss below in detail, this originates from the increasing topological constraints perpendicular to the pore wall.[16,17,19,49] In addition, pronounced narrowing of the distribution of chain modes is evident during the adsorption, as reflected by the increase in the high-frequency slope, mn, with time (Figure 4c). This could imply orientation effects for the subchains (e.g., perpendicular to the pore walls) that are dielectrically inactive.

To better understand the effect of molar mass on the adsorption kinetics, four PFs were employed (under the same conditions as that for the linear PIs i.e., $d = 100$ nm and $T = 303.15$ K). Despite theoretical work on the adsorption kinetics of linear polymers, and in particular, in predicting the molar mass dependence of the characteristic adsorption times,[8,50−55] to our knowledge there are not any experiments that discuss the corresponding scaling of combs and bottlebrushes. The

characteristic adsorption times of PF are compared to those of PI in a double-logarithmic plot against the reduced molar mass M_n/M_e in Figure 5.
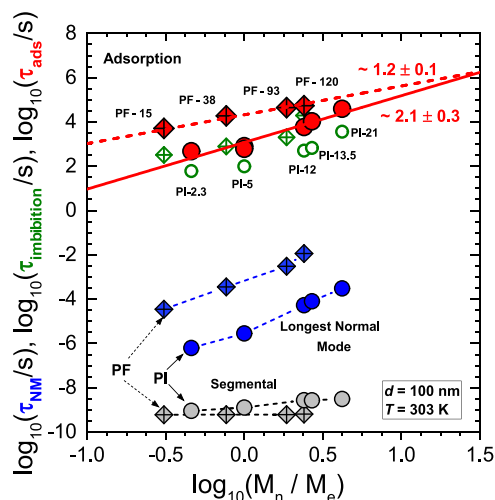
Figure 5. Logarithmic characteristic times (segmental: gray; longest normal mode: blue; imbibition times: green; adsorption: red) within AAO nanopores with a pore diameter of 100 nm, for both topologies (linear: circles, and bottlebrush: rhombi) as a function of the reduced molar mass to the respective entanglement molar mass. Uncertainties are typically smaller than the symbol size. The longest normal mode times were extracted at the end of the adsorption process. The dependence of the adsorption times differs in PI as compared to PF with respective slopes of 2.1 and 1.2. Open circles/rhombi give the characteristic imbibition times for PI and PF, respectively.

In the same plot, we show the imbibition times and the characteristic molecular times for the segmental and the longest normal modes. The latter time scale can be discussed based on the Rouse ($M_n < M_c \sim 2M_e$, where M_c is the critical molar mass) and the reptation theories ($M_n > M_c$). On the other hand, the adsorption times scale is much longer than any molecular time scale (over 10 orders of magnitude slower than the structural relaxation). From a theoretical perspective, the equilibrium of the system within the pores is attained through the balance of free energy (enthalpic contribution) and the formation of an interfacial (adsorbed) layer. According to the scaling theory developed by de Gennes, the adsorption of linear polymers on a flat surface is predicted to be a two-step process.[51,52] Initially, a chain to be adsorbed needs to overcome the potential barrier due to the excluded volume of the already adsorbed chains. Second, the incoming chain replaces the already adsorbed chains, whereas the previously adsorbed chain unfolds by the formation of long loops. It is envisaged that outgoing and incoming chains must pass through several unfavorable configurations; hence, the latter process was predicted to be very slow. The theory considers entangled polymers and suggests that the longest relaxation time scales as $\tau \sim \tau_s\, N^3$, where τ_s is the relaxation time of an adsorbed repeat unit. Subsequently, the theory was modified by Semenov and Joanny addressing the configurations of tails and loops within the adsorbed layer to predict the molar mass dependence of the adsorption and exchange time as $\tau_{\text{ads}} \sim N^{2.24}$ and $\tau_{\text{exc}} \sim N^{2.42}$, respectively.[55] Shaffer has studied the single-chain polymer adsorption dynamics to a strongly attractive surface using a generalization of the bond fluctuation model.[54] The adsorption was described by a "zipping"

process where the segments adsorb sequentially following the first adsorbed segment. The characteristic adsorption times were found to scale as $\tau_{ads} \sim N^{1.58}$.

Recent studies of the adsorption kinetics of linear and star-shaped PIs within nanoporous alumina (where confinement is 2-D) demonstrated that the adsorption times scale as $\tau_{ads} \sim N^{2.6}$ for both topologies.[17,19] For linear PIs, additional data obtained from refs 11,17 suggest $\tau_{ads} \sim N^{2.1\pm0.3}$ (Figure 5). This result is in agreement with scaling theories for linear entangled polymers. Coarse-grained simulations have demonstrated that the effect of adsorption is stronger for star polymers and is highly dependent on the number of arms.[30] Experimentally the adsorption times of multiarm star-shaped PIs ($f = 64$ arms, where f is the number of arms) were found to be about 2 orders of magnitude slower than the respective linear PI (for given $M_n^{arm} = M_n^{linear}$).[19] In the case of bottlebrush architecture (PF) the adsorption time scales as $\tau_{ads} \sim N_{bb}^{1.2\pm0.1}$, albeit with a greater uncertainty. Notice that, for a given M_n/M_e, the adsorption times of PFs are slower than that of PIs, but the different slopes suggest that there is a critical normalized molar mass where the trend is reversed. As we will discuss below in detail, the origin of PF weak dependence on molar mass could be explained in terms of the configurations on pore walls. When compared under a fixed molar mass, the adsorption kinetics of PF is faster than that of linear PI due to many free side chains that are not fully adsorbed.

The viscosity that a polymer experiences during flow in nanopores (η_{eff}) is expected to influence the adsorption process. From the unified theory of imbibition dynamics of entangled polymers developed by Doi and co-workers, it is known that polymer chains do not penetrate pores with their bulk viscosity.[14] Although the imbibition length follows the $t^{1/2}$ dependence, according to the LWE, the prefactor fails to describe the details of the process. Polymer imbibition was discussed by two mechanisms. For shorter chains or for larger pores, standard hydrodynamic flow prevails. Under a strong attraction by the pore walls, a layer of immobile chains is formed (called "dead" layer), resulting in an increase of the effective viscosity. For longer chains, reptation under a pressure gradient leads to a plug flow profile and a reduced effective viscosity. These results were confirmed by a series of experiments and simulations on linear and star-shaped polymers during their flow in cylindrical nanopores.[12,14−19,30]

Like earlier findings for linear PI, the effective viscosity of PF during flow in AAO is higher than that in bulk. The η_{eff} can be extracted from the LWE as $\eta_{eff} = \eta_0 \times (t_{peak}/t_{LW}) = t_{peak} \times (\gamma R_p \cos\theta/2L^2)$. The results for the molar mass dependence of the effective viscosity for linear PI[11] and the PF are shown in Figure 6a,b, whereas those for PI-stars[19] are shown in Figure S14. The effective viscosity for linear, star PI and the present bottlebrush PF scale as $\eta_{eff} \sim N^a$, where $a_{PI} = 2.3 \pm 0.2$, $a_{SPI} = 1.3 \pm 0.1$, and $a_{PF} = 1.7 \pm 0.6$, revealing that topology exerts a strong influence on hydrodynamic flow. The effect of the increasing η_{eff} on the adsorption time scales can be discussed with the help of Figure 6c, where τ_{ads} and η_{eff} are compared in a double-logarithmic plot for different topologies; linear, star PIs, and bottlebrush PFs for the same nanopores ($d = 100$ nm). The results have an approximate dependence of $\tau_{ads} \sim \eta_{eff}^{0.7}$ for the three topologies, suggesting a strong influence of the chain configurations within the adsorbed layer.

The adsorption kinetics of PFs are further discussed as a function of pore diameter with the help of Figure 7. The adsorption time together with the times of the two molecular
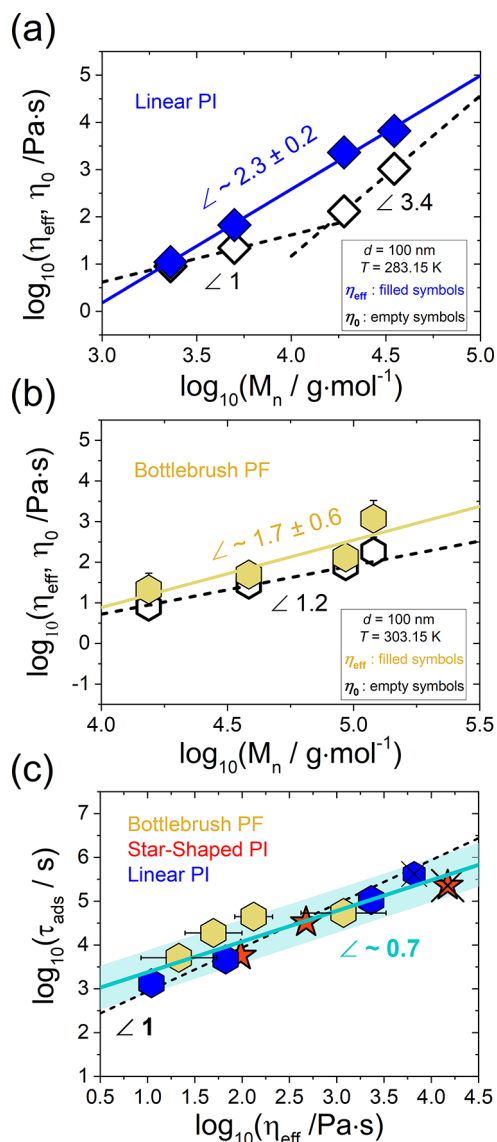
Figure 6. Logarithmic zero-shear (η_0 ; empty symbols) and effective (η_{eff} ; filled symbols) viscosities of (a) linear PI and (b) PF within nanoporous alumina with a pore diameter of 100 nm against the logarithmic molar mass. The zero-shear viscosity of both PI and PF scale with the molar mass to the power of 1.1 ($M < M_c$) and 3.4 ($M > M_c$). (a) The blue solid line is a linear fit to the logarithmic η_{eff} of PIs with a slope of 2.3. (b) The yellow solid line is a linear fit to the logarithmic η_{eff} of PFs with a slope of 1.7. (c) Adsorption time of the three different topologies (linear PI: blue hexagons, star-shaped PI: red stars $f = 64$, and PF: yellow hexagons) as a function of the effective viscosity in a double-logarithmic plot. The crossed symbols refer to the minimum adsorption time, as longer time scales are experimentally formidable. The solid line is a linear fit with a slope of 0.7. The black dashed line with a slope of 1 is to guide the eye.

processes, the longest normal mode and the segmental process of two PFs (PF-15; $M_n/M_e = 0.3$, and PF-120; $M_n/M_e = 2.6$) are compared to the respective times of the linear PI-5 ($M_n/M_e = 1$).[17] Starting from the faster relaxation process, we find that the segmental mobility is of the order of ns and remains d-invariant. The characteristic time of the longest normal mode, τ_{NM}, (chain mobility), was obtained at the end of the adsorption process. Within the smaller pores, the τ_{NM} of PFs is significantly longer than in bulk (Figure 4b). The slower chain relaxation under confinement demonstrates an increase
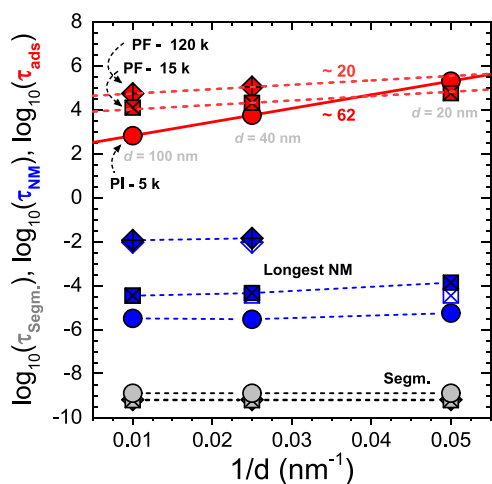
Figure 7. Logarithmic characteristic times (segmental: gray; longest normal mode: blue; and adsorption: red) within AAO nanopores for both topologies (linear: circles, and bottlebrush: rhombi and squares) as a function of the inverse pore diameter. Uncertainties are typically smaller than the symbol size. The dependence of the adsorption times is given by the slope of the linear line which is significantly smaller in PF. The characteristic time of the longest normal mode was extracted at the end of the adsorption process (filled blue symbols) and is compared to the bulk (open blue symbols).

of spatial constraints perpendicular to the surface due to loop and train configurations.[49] These constraints are more pronounced for longer and especially for well-entangled chains where loop threading is dominant, giving rise to a mobility gradient that "propagates" in the direction normal to the surface.

The adsorption time is about 14 orders of magnitude slower than the segmental relaxation and becomes gradually slower with decreasing pore diameter for both topologies. The pore size dependence of the adsorption time follows the empirical relation $\log_{10}(\tau_{ads}) \sim (\xi/d)$, where ξ (in nm) is a characteristic molar mass invariant parameter. Linear chains exhibit a stronger d dependence ($\xi_{PI} = 62$ nm),[17] with the adsorption time increasing by 2.5 orders of magnitude from $d = 100$ to $d = 20$ nm, in contrast to the weaker d dependence of PFs ($\xi_{PF} = 20$ nm) where the adsorption time increases roughly by an order of magnitude. For star polymers, the respective parameter is $\xi_{SPI} \sim 32$ nm ($f = 64$).[19]

Next, we investigated the temperature dependence of the characteristic adsorption times. The evolution of the dielectric loss curves and dielectric strength of PF-38 ($M_n/M_e \sim 0.8$) are presented in Figure S15. In Figure 8, we compare the characteristic adsorption times, τ_{ads}, of the bottlebrush PF-38 with the corresponding times for a regular star composed of 6 arms (SPI-6−2.6), a multiarm star PI composed of 64 arms (SPI-64−2.6), and a linear PI (PI-5) with an end-to-end distance comparable to the two stars ($2M_n^{SPI} \sim M_n^{PI-5} = M_e^{PI} = 5$ kg/mol). The data for the SPIs and the linear PI were obtained from previous studies.[11,19] For the SPI-6−2.6 additional measurements were performed at a temperature of $T = 273$ K (Figure S16, in the Supporting Information). The data in Figure 8, all within AAO templates with $d = 100$ nm, demonstrate a clear correlation between polymer topology and T dependence of τ_{ads}. The linear PI-5 shows the steeper temperature dependence, the two stars an intermediate dependence, and the bottlebrush PF-38 the weaker $\tau_{ads}(T)$. Furthermore, there is a dependence of $\tau_{ads}(T)$ on the number
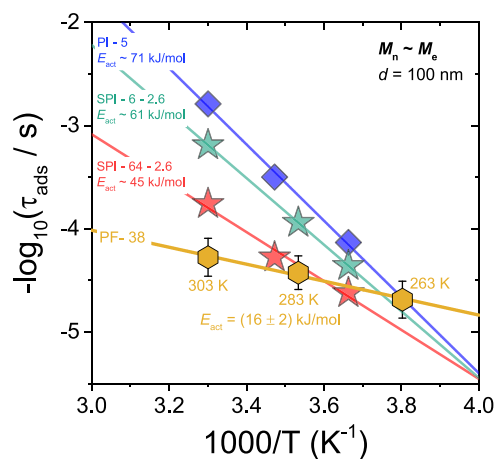

Figure 8. Inverse temperature dependence of the characteristic adsorption times of PF-38 (yellow symbols). Data for star-shaped (red and green) and linear (blue) polyisoprene, all with the same $M_n/M_e \sim 1$ are included for comparison. The solid lines represent fits to an Arrhenius dependence.

of arms for the two SPIs investigated. The results on the corresponding activation energies are shown in Table 2, in comparison to the activation energies for the segmental and local β-process operating within the same temperature range extracted through the Arrhenius dependence ($\tau_{ads} = \tau_\infty \exp[E_{act}/RT]$). As can be seen, the apparent activation energy shows a strong dependence on polymer topology (from 71 kJ/mol in linear PI-5 to 16 kJ/mol in the bottlebrush PF-40) in contrast to the activation energy for the segmental (and for the local β-process) that shows only a moderate dependence.

The difference in the apparent activation energies obtained from the adsorption process could be related to the binding energy. The latter was calculated in the framework of a mean field theory, for a dilute solution of polymers with different topologies.[8] It was shown that both a star and a comb-like polymer exhibit a lower binding energy as compared to a linear polymer. Furthermore, the binding energy was predicted to be inversely proportional to the star functionality, f. Both findings agree with the experimental data shown in Figure 8.

The measured energy is related to the polymer−surface number of contacts (N^*). Star polymers have an increased number of contacts with the surface; from $N^*_{linear} \approx N^{1/2}$ in linear polymers to $N^*_{star} \approx N_{arm}^{1/2} f^{1/2}$ in a regular star polymer.[56] The latter formula overlooks the soft colloidal nature of multiarm star polymers, expecting a nonmonotonic increase of N^*_{star} with f due to rising core segment density.[8,24,53] In the case of PF, the number of contacts with the surface is always higher than for a linear chain due to the side chain and excluding volume effects.[56] As a result, the higher number of contacts of PFs affects the probability of a chain to detach from the surface indicating lower apparent activation energy.[8]

A detailed Monte Carlo simulation for a coarse-grained model of cylindrical brushes (backbone length, N_{bb}, side-group length, N_{sc}) adsorbed on a flat substrate revealed some unanticipated features. Under good solvent conditions the case of (~10% of adsorbed repeat units) and strong adsorption (~40% of adsorbed repeat units) were studied.[7] Varying N_{bb} and N_{sc} changes the overall size and stiffness. Under strong adsorption conditions, the backbone was forced to an almost 2D configuration. However, the transition from the weakly to strongly adsorbed state only slightly affected the side-group
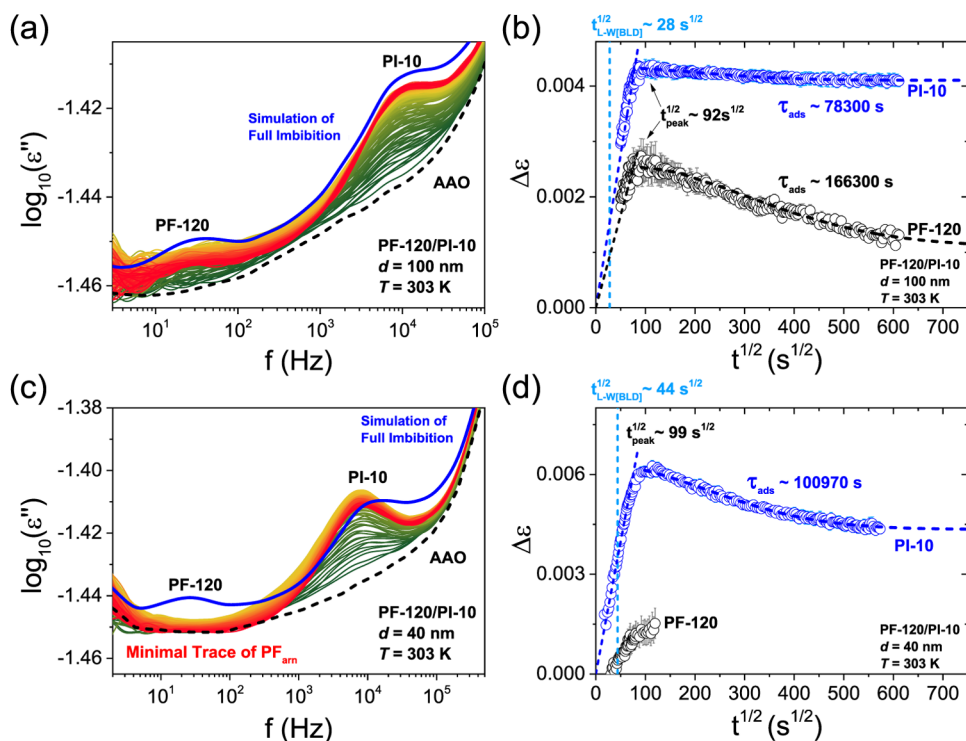
Figure 9. Evolution of dielectric loss curves of the mixture PF-120/PI-10 during imbibition (green curves) and following adsorption (yellow to red curves) within AAO nanopores with a pore diameter of (a) 100 nm and (c) 40 nm at a temperature of 303.15 K. (a) The two peaks correspond to the longest normal mode of the respective components in the blend. The black dashed line gives the signal of the empty template. The blue line is the expected blend signal at full imbibition based on eq 7. (c) The respective peak of PI-10 is intense, whereas there is a minimal trace of the PF component. (b) The respective dielectric strength of the two components as a function of the square root of time at $d = 100$ nm. The vertical light blue dashed line corresponds to the complete infiltration time according to Lucas−Washburn equation employing the zero-shear viscosity of the blend. (d) Evolution of the dielectric strength for the PI component in the blend. The black circles give an estimation of the dielectric strength of much weaker signal corresponding to the PF component. The thick dashed lines in (b, d), respectively, represent fits to an exponential decay function.

configuration. While a large fraction of the backbone repeats (>60%) were adsorbed, only a small fraction of side-group repeat units were found to be adsorbed and the fraction decreased while increasing N_{sc}.

These simulation results suggested that the number of contacts of a bottlebrush polymer scale as $\sim N_{sc}^{1/2} N_{bb}^{1/2}$, is only an approximation, and the true number of adsorbed units depends strongly on the strength of interactions on top of the N_{sc} and N_{bb} values. The number of contacts of a regular comb polymer was calculated in detail by Kosmas.[56] According to this, the number of contacts is given as a function of the total molecular mass as $M = N_{bb} + q N_{sc}$ (where q is the number of side chains, in the case of PFs, there is one side chain per monomer; $q = N_{bb}$) and the characteristic ratio $\rho = N_{sc}/N_{bb}$ which varies between the two limits; $\rho \to 0$ of the linear chain and $\rho \to \infty$ of the star chains. Thus, the explicit formula for the number of contacts is

$$N_{brush}^* \approx N_{bb}^{1/2}(1 + N_{sc})^{1/2}\left[\left(\frac{1}{1 + q\rho}\right)^{3/2}(1 + q\rho^{3/2})\right.$$

$$\left. + 2F(q, \rho)\right]$$

where $F(q,\rho)$ is a function that contains a summation from $k = 1$ to $k = q$. For the PF-40 ($N_{bb} = 201$ & $N_{sc} = 2$), we found that

$F(q,\rho) \approx 1$ (due to $\rho \ll 1$) and $[\left(\frac{1}{1 + q\rho}\right)^{3/2}(1 + q\rho^{3/2})] \approx 0.231$; hence, the total number of contacts is $N_{PF-38}^* \approx 55$. The activation energy for adsorption and the number of contacts for each topology are given together with the characteristic activation energy for the segmental α (Figure S17, in the Supporting Information) and β processes in Table 2.

In addition, the activation energy for adsorption can be compared to the energy of adhesion of a polymer. The latter is $E_{adh} = \left(\frac{N_A}{N^*}\right) \times S_{pol} \times W_{adh}$. Here, S_{pol} is the occupied area of a polymer on the substrate and W_{adh} is the work of adhesion defined as $W_{adh} = \gamma_{SL}(1 + \cos\theta_0)$.[19,23] Here, γ_{SL} is the interfacial energy ($\gamma_{SL} = \gamma_{SV} - \gamma_{LV}\cos\theta_0$; γ_{SV} is the solid−air interfacial energy, γ_{LV} is the liquid surface tension, and θ_0 is Young's contact angle). For linear PIs, E_{adh} is lower than the activation energy for adsorption. Evidently, the activation energy for adsorption, apart from the number of contacts, includes entropic factors related to the chain configurations next to the pore surface.

3.3. Imbibition Dynamics of Symmetric PF/PI Blends. Herein we explore the possibility of separating symmetrical PF/PI blends during imbibition and subsequent adsorption into nanopores. Earlier studies of linear binary blends of PIs have shown the possibility to separate the two components by employing the difference in imbibition speed and adsorption kinetics.[17] A recent study has examined the case of binary blends of different architecture, star-shaped *vs* linear PIs, and

demonstrated the possibility to separate the components of the different topology.[19] In the majority of cases, the polymer with the lower zero-shear viscosity in the melt infiltrated first the nanochannels, while both constituents exhibited slower adsorption kinetics with respect to their homopolymers. This situation gave rise to what is known as "topology sorting", *e.g.*, the separation of linear/star blend components without the use of solvent.

The evolution of the dielectric loss curves of the symmetrical blend PF-120/PI-10 during imbibition and following adsorption within AAO nanopores with a pore diameter of 100 nm is shown in Figure 9a. The master curves of the frequency-dependent storage (G') and loss (G'') moduli together with the T dependence of the zero-shear viscosity of the investigated blends are presented in Figures S18–S22. The two maxima in Figure 9a correspond to the longest normal mode of each component. The same graph shows the expected dielectric loss curve, ε''_{tot}, corresponding to the full imbibition, by employing the measured ε''_{AAO} and ε''_{pol} (in bulk) (eq 7). The "expected" dielectric loss curve in the blend is in good agreement with the experimental result following full imbibition, suggesting that both components infiltrate the nanopores. From the analysis of each curve, by fitting the data to a summation of two Havriliak–Negami equations for each component, the time evolution of the respective $\Delta\varepsilon$ was extracted and is plotted as a function of time in Figure 9b. Due to the difference in zero-shear viscosity of each component, η_{PF} ($\sim$183 Pa·s) > η_{PI} ($\sim$12 Pa·s), and the large size of the nanopores, ($2R_g^{PF-120}/d \sim 0.39$) both blend components infiltrate the nanopores. Following full imbibition, adsorption for both components is observed, with the PF presenting a reduction in $\Delta\varepsilon(t)$. The characteristic adsorption times for both blend components within the 100 nm nanopores ($\tau_{PI-120} \sim 166{,}000$ s and $\tau_{PI-10} \sim 78{,}300$ s) are slower than those of the respective homopolymers under the same conditions ($\tau_{PI-120} \sim 53{,}400$ s and $\tau_{PI-10} \sim 4470$ s). Apparently, the adsorption process is slowed down by the longer imbibition process.

By reducing the pore diameter from 100 to 40 nm ($2R_g^{PF-120}/d \sim 0.39$), differences in the imbibition and adsorption kinetics of the two components become evident. The dielectric loss curves of the binary blend as a function of time within the $d = 40$ nm nanopores together with the expected dielectric loss curve at the complete imbibition are shown in Figure 9c. Clearly, the component with the lower zero-shear viscosity in the bulk ($\eta_{PI} \sim 12$ Pa·s) penetrates faster the nanopores and adsorbs on the surface first. Only a minimum of PF-120 penetrates the pores, as evidenced by the respective dielectric strengths (Figure 9d). Nevertheless, the characteristic adsorption time of PI-10 is still much slower ($\tau_{PI-10} \sim 101{,}000$ s) than the respective time of the homopolymer ($\tau_{PI-10} \sim 22{,}000$ s). Demixing driven by the capillary action slows the dynamics and adsorption of PI-10. These effects are shown in a pictorial way in Figure 10.

Subsequently, we investigated the role of the size of the linear PI on the blend imbibition and adsorption process (results are shown in Figures S23 and S24) by investigating a symmetric PF-120/PI-18 blend within 40 nm nanopores. The results confirmed the "topology sorting" found with the PF-120/PI-10 blend.

Lastly, we examine the opposite case, in which the bottlebrush polymer (PF) is much smaller in size than the linear polymer (PI) (*i.e.*, $\eta_{PF} < \eta_{PI}$). The evolution of dielectric loss curves for the blend PI-38/PF-4 ($\eta_{PI} \sim 430$ Pa·s
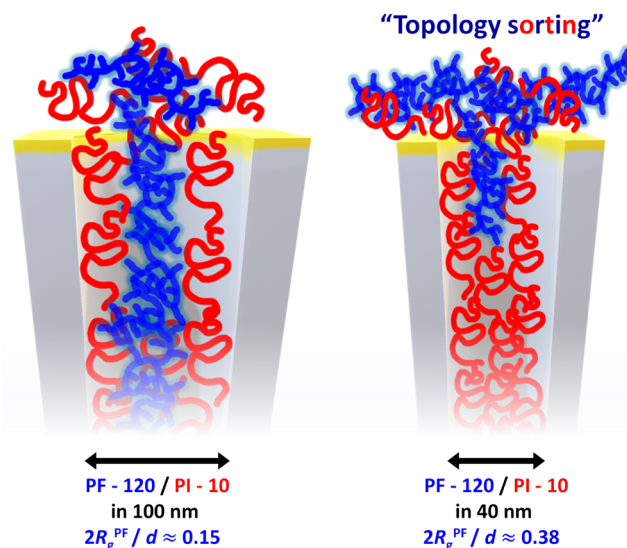

Figure 10. Highly schematic representation of the imbibition process for the PF-120/PI-10 binary blend. In the smaller nanopores, topology sorting takes place.

$\gg \eta_{PF} \sim 1$ Pa·s) are shown in Figure 11a. An inspection of the figure reveals that nanopores are initially enriched by the smaller size component (PF), whereas the larger PI-38 infiltrates the pores at much longer times, giving rise again to "topology sorting". In addition, a significant change in the distribution of relaxation times with time for the linear PI is evident as well as a shift of the longest normal mode to lower frequencies, *e.g.*, the characteristic relaxation times become slower with imbibition time (see Figure S25, in the Supporting Information). The adsorption times of the blend components are different from those of the corresponding components in the bulk. The adsorption times for the PF-4 is $\sim$3900 s, *i.e.*, much longer than the homopolymer (an exact value is not possible to extract due to the fast imbibition). On the other hand, the adsorption time for the PI-38 component in the blend is $\sim$ 45,000 s, *i.e.*, shorter than for the homopolymer adsorption ($\tau_{PI-38} \sim 275{,}000$ s). Evidently, the globular PF-4 dilutes the entanglements of PI-38 and speeds up the imbibition and adsorption processes. Additional examples of imbibition/adsorption in large pores are provided in Figure S26, Supporting Information.

4. CONCLUSIONS

The imbibition process of a model bottlebrush polymer (*cis*-1,4-polyfarnesene, PF) comprising short side chains of the same chemistry as in the backbone was monitored by following the evolution of normal modes during flow in nanopores. The process followed the $t^{1/2}$ dependence, as predicted by the Lucas–Washburn equation. Bottlebrush polymers penetrated into nanopores with a higher effective viscosity than bulk (when $2R_g < d$). A similar imbibition had been observed previously with linear and star polymers, which were brought in contact with the same nanopores. This reflects the formation of an adsorbed layer (dead layer) as predicted by theory and verified experimentally.[14] Moreover, we noticed some specific changes in the "spectrum" of normal modes during flow: (a) the narrowing of the distribution of relaxation times, especially from the high-frequency side (where the shorter normal modes) and (b) the average relaxation times for the longest normal mode being slower than bulk. Although the latter can
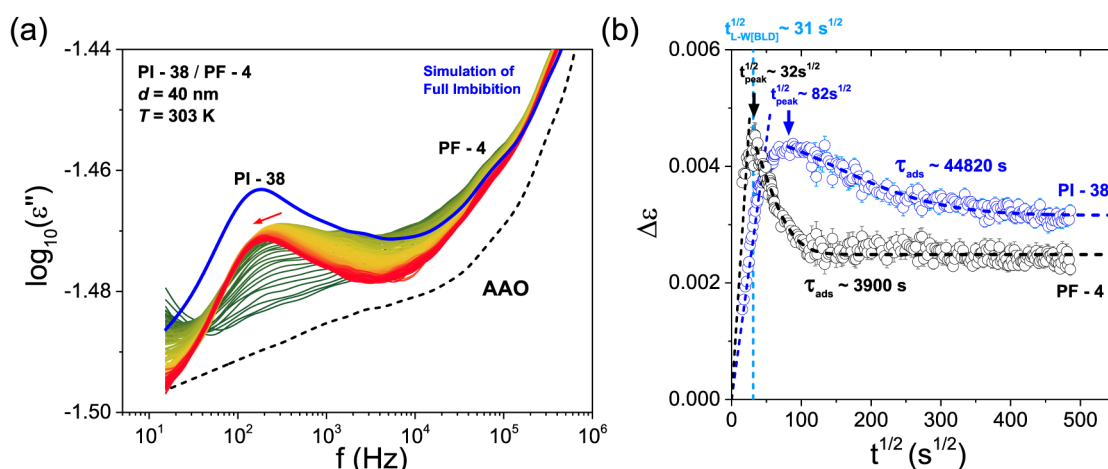
Figure 11. (a) Evolution of dielectric loss curves of the mixture PF-4/PI-38 during imbibition within AAO nanopores with a pore diameter of 40 nm at a temperature of 303.15 K. The two peaks correspond to the longest normal mode of the respective components in the blend. The black dashed line corresponds to the signal of the empty template. The blue thick line is the expected signal at complete imbibition based on eq 7. A shift to lower frequencies of the peak of PI-38 is evident during the adsorption. (b) The respective dielectric strength of PI-38 (blue) and PF-4 (black) components. Differences in both the imbibition and adsorption kinetics of the components are evident.

be explained by an increasing number of topological constraints (*e.g.*, entanglements) perpendicular to the pore walls, for the former we cannot provide an explanation, at present. Further work is necessary by both experiment and simulation to fully address the changes in molecular dynamics.

The adsorption time scales for bottlebrushes were much longer than any molecular process, being ~14 and ~8 orders of magnitude slower than the segmental and longest normal modes, respectively. The ultraslow time scales at a temperature of ~100 K above the glass temperature agree with earlier findings for the adsorption process in linear and star-shaped polymers. However, bottlebrush polymers exhibit even slower adsorption with characteristic time scales having a weak molar mass $(\tau_{ads} \sim N_{bb}^{1.2\pm0.1})$, pore size $(\log(\tau_{ads}) \sim \xi/d, \xi = 20$ nm), and temperature $(E_{act} \sim 16 \pm 2$ kJ/mol) dependence. These findings are discussed in terms of an increased number of contacts of the bottlebrush polymer with the surface.

Lastly, we take advantage of the difference in imbibition and adsorption speeds of bottlebrush polymers with respect to other topologies and demonstrate the separation of symmetric and athermal PF/PI blends to their constituent components in the absence of solvent.

■ ASSOCIATED CONTENT

ⓈⒾ Supporting Information

The Supporting Information is available free of charge at https://pubs.acs.org/doi/10.1021/acs.macromol.4c02952.

> Additional dielectric and rheological data in the bulk; comparison of dielectric spectra and distribution of relaxation times; and further *in situ nDS* results (PDF)

■ AUTHOR INFORMATION

Corresponding Author

George Floudas − *Department of Physics, University of Ioannina, 45110 Ioannina, Greece; Max Planck Institute for Polymer Research, 55128 Mainz, Germany; University Research Center of Ioannina (URCI)−Institute of Materials Science and Computing, 45110 Ioannina, Greece;* ◉ orcid.org/0000-0003-4629-3817; Email: gfloudas@uoi.gr

Authors

Panagiotis Kardasis − *Department of Physics, University of Ioannina, 45110 Ioannina, Greece*

Ioannis Tzourtzouklis − *Department of Physics, University of Ioannina, 45110 Ioannina, Greece*

Yun Dong − *Max Planck Institute for Polymer Research, 55128 Mainz, Germany*

Moritz Meier-Merziger − *Department of Chemistry, Johannes Gutenberg University Mainz, 55128 Mainz, Germany*

Hans-Jürgen Butt − *Max Planck Institute for Polymer Research, 55128 Mainz, Germany;* ◉ orcid.org/0000-0001-5391-2618

Holger Frey − *Department of Chemistry, Johannes Gutenberg University Mainz, 55128 Mainz, Germany;* ◉ orcid.org/0000-0002-9916-3103

Complete contact information is available at:
https://pubs.acs.org/10.1021/acs.macromol.4c02952

■ REFERENCES

(1) Granick, S. Motions and Relaxations of Confined Liquids. *Science* **1991**, *253*, 1374−1379.

(2) Johnson, H. E.; Douglas, J. F.; Granick, S. Topological Influences on Polymer Adsorption and Desorption Dynamics. *Phys. Rev. Lett.* **1993**, *70*, No. 3267.

(3) Douglas, J. F.; Johnson, H. E.; Granick, S. A Simple Kinetic Model of Polymer Adsorption and Desorption. *Science* **1993**, *262*, 2010−2012.

(4) Napolitano, S.; Wübbenhorst, M. The Lifetime of the Deviations from Bulk Behaviour in Polymers Confined at the Nanoscale. *Nat. Commun.* **2011**, *2*, No. 260.

(5) Paturej, J.; Sheiko, S. S.; Panyukov, S.; Rubinstein, M. Molecular Structure of Bottlebrush Polymers in Melts. *Sci. Adv.* **2016**, *2*, No. e1601478.

(6) Hsu, H.-P.; Paul, W.; Binder, K. Conformational Studies of Bottle-Brush Polymers Absorbed on a Flat Solid Surface. *J. Chem. Phys.* **2010**, *133*, No. 134902.

(7) Hsu, H.-P.; Paul, W.; Binder, K. Structure of Bottle Brush Polymers on Surfaces: Weak versus Strong Adsorption. *J. Phys. Chem. B* **2011**, *115*, 14116−14126.

(8) Joanny, J. F.; Johner, A. Adsorption of Polymers with Various Architectures: Mean Field *Theory. J. Phys. II* **1996**, *6*, 511−527.

(9) Xie, R.; Mukherjee, S.; Levi, A. E.; Reynolds, V. G.; Wang, H.; Chabinyc, M. L.; Bates, C. M. Room Temperature 3D Printing of Super-Soft and Solvent-Free Elastomers. *Sci. Adv.* **2020**, *6*, No. eabc6900.

(10) Peng, X.; Wang, X.; Zhou, X.; Lin, Z.; Zeng, F.; Huang, X. Lab-on-a-Chip Systems in Imbibition Processes: A Review and Applications/Issues for Studying Tight Formations. *Fuel* **2021**, *306*, No. 121603.

(11) Kardasis, P.; Tzourtzouklis, I.; Nega, A. D.; Sakellariou, G.; Steinhart, M.; Floudas, G. Topology Sorting: Separating Linear/Star Polymer Blend Components by Imbibition in Nanopores. *J. Chem. Phys.* **2024**, *160*, No. 044912.

(12) Yao, Y.; Butt, H.-J.; Zhou, J.; Doi, M.; Floudas, G. Capillary Imbibition of Polymer Mixtures in Nanopores. *Macromolecules* **2018**, *51*, 3059−3065.

(13) Morrow, N. R.; Mason, G. Recovery of Oil by Spontaneous Imbibition. *Curr. Opin. Colloid Interface Sci.* **2001**, *6*, 321−337.

(14) Yao, Y.; Butt, H.-J.; Floudas, G.; Zhou, J.; Doi, M. Theory on Capillary Filling of Polymer Melts in Nanopores. *Macromol. Rapid Commun.* **2018**, *39*, No. e1800087.

(15) Tu, C.-H.; Steinhart, M.; Butt, H.-J.; Floudas, G. In Situ Monitoring of the Imbibition of Poly(n-Butyl Methacrylates) in Nanoporous Alumina by Dielectric Spectroscopy. *Macromolecules* **2019**, *52*, 8167−8176.

(16) Tu, C.-H.; Zhou, J.; Doi, M.; Butt, H.-J.; Floudas, G. Interfacial Interactions during in Situ Polymer Imbibition in Nanopores. *Phys. Rev. Lett.* **2020**, *125*, No. 127802.

(17) Tu, C.-H.; Zhou, J.; Butt, H.-J.; Floudas, G. Adsorption Kinetics of Cis-1,4-Polyisoprene in Nanopores by in Situ Nanodi-electric Spectroscopy. *Macromolecules* **2021**, *54*, 6267−6274.

(18) Tu, C.-H.; Steinhart, M.; Berger, R.; Kappl, M.; Butt, H.-J.; Floudas, G. When Crystals Flow. *Sci. Adv.* **2023**, *9*, No. eadg8865.

(19) Kardasis, P.; Sakellariou, G.; Floudas, G. Ultraslow Adsorption of Star *cis*-1,4-Polyisoprenes by in Situ Imbibition in Nanopores. *Macromolecules* **2024**, *57*, 481−489.

(20) Serghei, A.; Chen, D.; Lee, D. H.; Russell, T. P. Segmental Dynamics of Polymers during Capillary Flow into Nanopores. *Soft Matter* **2010**, *6*, 1111−1113.

(21) Yao, Y.; Alexandris, S.; Henrich, F.; Auernhammer, G.; Steinhart, M.; Butt, H.-J.; Floudas, G. Complex Dynamics of Capillary Imbibition of Poly(Ethylene Oxide) Melts in Nanoporous Alumina. *J. Chem. Phys.* **2017**, *146*, No. 203320.

(22) Hor, J. L.; Wang, H.; Fakhraai, Z.; Lee, D. Effect of Physical Nanoconfinement on the Viscosity of Unentangled Polymers during Capillary Rise Infiltration. *Macromolecules* **2018**, *51*, 5069−5078.

(23) Alexandris, S.; Papadopoulos, P.; Sakellariou, G.; Steinhart, M.; Butt, H.-J.; Floudas, G. Interfacial Energy and Glass Temperature of Polymers Confined to Nanoporous Alumina. *Macromolecules* **2016**, *49*, 7400−7414.

(24) Kardasis, P.; Oikonomopoulos, A.; Sakellariou, G.; Steinhart, M.; Floudas, G. Effect of Star Architecture on the Dynamics of 1,4-Cis-Polyisoprene under Nanometer Confinement. *Macromolecules* **2021**, *54*, 11392−11403.

(25) Thoms, E.; Song, Z.; Wang, K.; Napolitano, S. Simple Model to Predict the Adsorption Rate of Polymer Melts. *Phys. Rev. Lett.* **2024**, *132*, No. 248101.

(26) De Gennes, P.-G.; Brochard-Wyart, F.; Quere, D. *Capillarity and Wetting Phenomena: Drops, Bubbles, Pearls, Waves*; Springer: New York, NY, 2010.

(27) Johner, A.; Shin, K.; Obukhov, S. Nanofluidity of a Polymer Melt: Breakdown of Poiseuille's Flow Model. *Europhys. Lett.* **2010**, *91*, No. 38002.

(28) Dimitrov, D. I.; Milchev, A.; Binder, K. Capillary Rise in Nanopores: Molecular Dynamics Evidence for the Lucas-Washburn Equation. *Phys. Rev. Lett.* **2007**, *99*, No. 054501.

(29) Zhang, J.; Lei, J.; Tian, W.; Zhang, G.; Floudas, G.; Zhou, J. Capillary Filling of Polymer Chains in Nanopores. *Macromolecules* **2023**, *56*, 2258−2267.

(30) Zhang, J.; Lei, J.; Feng, P.; Floudas, G.; Zhang, G.; Zhou, J. Capillary Filling of Star Polymer Melts in Nanopores. *J. Chem. Phys.* **2024**, *160*, No. 054903.

(31) Patsalidis, N.; Papamokos, G.; Floudas, G.; Harmandaris, V. Understanding the Interaction between Polybutadiene and Alumina via Density Functional Theory Calculations and Machine-Learned Atomistic Simulations. *J. Phys. Chem. C* **2022**, *126*, 16792−16803.

(32) Patsalidis, N.; Papamokos, G.; Floudas, G.; Harmandaris, V. Structure and Dynamics of a Polybutadiene Melt Confined between Alumina Substrates. *Macromolecules* **2023**, *56*, 6552−6564.

(33) Patsalidis, N.; Papamokos, G.; Floudas, G.; Harmandaris, V. Temperature Dependence of the Dynamics and Interfacial Width in Nanoconfined Polymers via Atomistic Simulations. *J. Chem. Phys.* **2024**, *160*, No. 104904.

(34) van der Linden, C. C.; Leermakers, F. A. M.; Fleer, G. J. Adsorption of Comb Polymers. *Macromolecules* **1996**, *29*, 1000−1005.

(35) Iacob, C.; Yoo, T.; Runt, J. Molecular Dynamics of Polyfarnesene. *Macromolecules* **2018**, *51*, 4917−4922.

(36) Tzourtzouklis, I.; Hahn, C.; Frey, H.; Floudas, G. Molecular Dynamics and Viscoelastic Properties of the Biobased 1,4-Polymyrcene. *Macromolecules* **2022**, *55*, 8766−8775.

(37) Tzourtzouklis, I.; Meier-Merziger, M.; Frey, H.; Floudas, G. Supersoft Polymer Melts in Binary Blends of Bottlebrush Cis-1,4-polyfarnesene and Cis-1,4-polyisoprene. *Macromol. Rapid Commun.* **2024**, *45*, No. 2400551.

(38) Meier-Merziger, M.; Fuchs, D. A. H.; Frey, H.; Müller, A. H. E. Spotlight on Methyl tert-Butyl Ether—Underrated or Overlooked? Unveiling Its Role for Living Anionic Polymerization. *Macromolecules* **2024**, *57*, 8154−8161.

(39) Meier-Merziger, M.; Imschweiler, J.; Hartmann, F.; Niebuur, B.-J.; Kraus, T.; Gallei, M.; Frey, H. Bifunctional Carbanionic Synthesis of Fully Bio-Based Triblock Structures Derived from β-Farnesene and LL-Dilactide: Thermoplastic Elastomers. *Angew. Chem., Int. Ed.* **2023**, *62*, No. e202310519.

(40) Stockmayer, W. H. Dielectric dispersion in solutions of flexible polymers. *Pure Appl. Chem.* **1967**, *15*, 539−554.

(41) Fetters, L. J.; Lohse, D. J.; Colby, R. H. *Physical Properties of Polymers Handbook*; Springer New York: New York, NY, 2007; pp 447−454.

(42) *Broadband Dielectric Spectroscopy*; Kremer, F.; Schoenhals, A., Eds.; Springer: Berlin, Germany, 2012.

(43) Suzuki, Y.; Duran, H.; Steinhart, M.; Kappl, M.; Butt, H.-J.; Floudas, G. Homogeneous Nucleation of Predominantly Cubic Ice Confined in Nanoporous Alumina. *Nano Lett.* **2015**, *15*, 1987−1992.

(44) Duran, H.; Steinhart, M.; Butt, H.-J.; Floudas, G. From heterogeneous to homogeneous nucleation of isotactic poly-(propylene) confined to nanoporous alumina. *Nano Lett.* **2011**, *11*, 1671−1675.

(45) Spyridakou, M.; Maji, T.; Gkikas, M.; Ngai, K. L.; Floudas, G. Sub-Rouse Dynamics in Poly(Isobutylene) as a Function of Molar Mass. *Macromolecules* **2021**, *54*, 9091−9099.

(46) Mapesa, E. U.; Popp, L.; Kipnusu, W. P.; Tress, M.; Kremer, F. Molecular Dynamics in 1- and 2-D Confinement as Studied for the Case of Poly(Cis-1,4-Isoprene). *Soft Mater.* **2014**, *12*, S22−S30.

(47) Lucas, R. Ueber das Zeitgesetz des kapillaren Aufstiegs von Flüssigkeiten. *Colloid Polym. Sci.* **1918**, *23*, 15−22.

(48) Washburn, E. W. The dynamics of capillary flow. *Phys. Rev.* **1921**, *17*, No. 273.

(49) Granick, S. Perspective: Kinetic and Mechanical Properties of Adsorbed Polymer Layers. *Eur. Phys. J. E* **2002**, *9*, 421−424.

(50) de Gennes, P. G. Scaling Theory of Polymer Adsorption. *J. Phys.* **1976**, *37*, 1445−1452.

(51) de Gennes, P. G. Polymer Solutions Near an Interface. Adsorption and Depletion Layers. *Macromolecules* **1981**, *14*, 1637−1644.

(52) de Gennes, P. G. Polymers at an Interface; a Simplified View. *Adv. Colloid Interface Sci.* **1987**, *27*, 189−209.

(53) Halperin, A.; Joanny, J. F. Adsorption of Star Polymers. *J. Phys. II* **1991**, *1*, 623−636.

(54) Shaffer, J. S. Computer Simulation of Homopolymer and Copolymer Adsorption Dynamics. *Macromolecules* **1994**, *27*, 2987−2995.

(55) Semenov, A. N.; Joanny, J.-F. Kinetics of Adsorption of Linear Homopolymers onto Flat Surfaces: Rouse Dynamics. *J. Phys. II* **1995**, *5*, 859−876.

(56) Kosmas, M. K. Ideal Polymer Chains of Various Architectures at a Surface. *Macromolecules* **1990**, *23*, 2061−2065.